**An article presented by Prof. Monalisa Mukherjee *et al*. of Amity Institute of Click Chemistry Research and Studies, Amity University, Noida, India.**

Sustainable synthesis of single crystalline sulphur-doped graphene quantum dots for bioimaging and beyond

Waste-driven single crystalline sulphur-doped GQDs synthesized *via* green hydrothermal route with highest quantum yield bearing excellent biocompatibility for bioimaging.
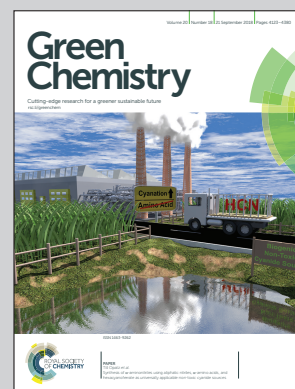
ROYAL SOCIETY OF CHEMISTRY

rsc.li/greenchem

Green Chemistry

PAPER

Sustainable synthesis of single crystalline sulphur-doped graphene quantum dots for bioimaging and beyond†

Sujata Sangam, ‡[a] Apoorv Gupta, ‡[a] Adeeba Shakeel, §[a] Rohan Bhattacharya, §[a] Arun Kumar Sharma, [b] Deepa Suhag, [c] Sandip Chakrabarti, [d] Sandeep Kumar Garg, [e] Sourav Chattopadhyay, [f] Biswarup Basu, [a] Vinod Kumar, [g] Satyendra Kumar Rajput, [b] Malay Kishore Dutta [h] and Monalisa Mukherjee *[a,c]

The ongoing race of biomedical applications has given momentum to the development of graphene quantum dots (GQDs). GQDs are zero-dimensional fluorescent carbon-nanomaterials, with a pronounced quantum confinement effect, and abundant edge states and functional groups. Despite their potential applications, mass-scale synthesis of single crystalline graphene quantum dots (GQDs) with high quantum yields derived *via* a direct green synthesis approach from bio-wastes is a major challenge. Hitherto, green extract (*i.e.* sugarcane molasses) driven single crystalline sulphur-doped GQDs (S-GQDs) with a longer decay time, high quantum yield, and excellent biocompatibility have remained unexplored in the bioimaging arena. At the same time, this agro-industrial waste has value in terms of both products and byproducts *i.e.* zero waste generation resulting in reduced human footprint on the environment. For the first time, we present a facile, large-scale, one-step, economical, template- and catalyst-free synthesis of sustainable, highly crystalline S-GQDs *via* a hydrothermal route from second generation (2G) bio-wastes. Mechanistic insight into the formation of S-GQDs from their precursor was obtained using powder X-ray diffraction patterns (PXRD). S-GQDs directly obtained from bio-wastes without surface passivation showed the highest quantum yield (QY) ~ 47% obtained to date. The wide and symmetric emission spectrum of these S-GQDs is instrumental for sensitive detection as labelling nanoprobes. Moreover, their non-toxic behavior, *in vitro* and *in vivo*, has a future in quick point-of-care screening and real-time bioimaging. Thus, the as-synthesized bio-waste derived S-GQDs accomplished the purpose of an advanced environmentally friendly and sustainable material which is non-toxic, viable, safe, and cheap. This unprecedented work advances the synthesis of high-quality S-GQDs from bio-waste, which provides a breakthrough in the bioimaging field.

[a]Biomimetic and Nanostructured Materials Research Laboratory, Amity Institute of Biotechnology, Amity University, Uttar Pradesh, Sector-125, Noida, India. E-mail: mmukherjee@amity.edu; Tel: +91(0)-120-4392194, +91(0)-120-503 4586945
[b]Amity Institute of Pharmacy, Amity University, Uttar Pradesh, 201303, India
[c]Amity Institute of Click Chemistry Research and Studies, Amity University, Uttar Pradesh, 201303 Noida, India
[d]Amity Institute of Nanotechnology, Amity University, Uttar Pradesh, 201303, India
[e]PG Department of Physics, Patna University, Bihar-800005, India
[f]Department of Electronics, Ramakrishna Mission Residential College, Narendrapur, Kolkata-700103, India
[g]Amity Institute of Applied Sciences, Amity University, Uttar Pradesh, 201303, India
[h]Amity School of Engineering and Technology, Amity University, Uttar Pradesh, 201303, India
†Electronic supplementary information (ESI) available: Fig. S1–S10, Tables S1–S5 and supplementary references. See DOI: 10.1039/c8gc01638k
‡These authors contributed equally as the first author.
§These authors contributed equally as the second author.

Introduction

The necessity to apply an environmentally friendly and renewable raw material source is of paramount importance in coping with the alarming challenges facing the sustainable production of nanomaterials without using hazardous ingredients. These challenges could be overcome by developing graphene quantum dots (GQDs) based on green technology, which is at the core of sustainability. Versatile GQDs have been proposed for a cornucopia of diverse biomedical applications with great promise in the field of bioimaging[1–3] due to their unique photostability, tunable surface functionalities, and benign nature.[4–9] GQDs are 0-dimensional (0D),[1] sp²-hybridized, typically 1–3 atomic layer thick, multifunctional, and fluorescent semiconductor nanocrystals lying at the junction

of graphene and quantum dots.[3,4,9–13] Essentially, their optical properties have been inextricably intertwined by the quantum confinement effect[2] along with high charge mobility, tunable conductance, and band gap.[13–16] This quantum confinement effect can be observed in the size range of 1–10 nm.[6,14]

Several methods have been used to synthesize GQDs; however, most of them are either tedious or non-environmentally friendly and the source materials are often expensive.[16–19] Recently, a lot of focus has been put on second generation (2G) waste utilization; however, until now, there have been limited studies using bio-wastes for the synthesis of GQDs. Wang *et al.*, Suryawanshi *et al.*, Xue *et al.*, and Ding *et al.* reported that GQDs were synthesized from rice husk (QY 8.1%), neem leaves (QY 1–2%), peanut shells (QY 9.91%), and lignin biomass (QY 21%), respectively.[20–23] Liu *et al.* and Lu *et al.* reported GQDs and graphene oxide quantum dots using triethylenetetramine with *p*-benzoquinone and black carbon with H_2O_2 as reagents with a QY of ∼ 17.5 and ∼ 4.13%, respectively.[24,25] Unfortunately, only a very low quantum yield (usually <25%) could be achieved from waste biomass, severely limiting their use in a myriad of applications.[20–22] Ding *et al.* reported the synthesis of single-crystalline GQDs from lignin biomass that involved the use of corrosive chemicals such as nitric acid for 12 h *via* a two-step method.[23] Similarly, G. Wang's group prepared S-GQDs from durian fruit with a relatively higher QY, devoid of single crystallinity, using very expensive platinum sheets as the catalyst in 12 h.[26] However, no literature is available to date on a single step, mass-scale, template- and catalyst-free synthesis of single crystalline sulphur doped graphene quantum dots (S-GQDs) from bio-wastes without surface passivation affording high QYs as well as comprehensive utilization of the products. These above facts kindled us to synthesize hydrophilic S-GQDs from a low cost, single source precursor and to decipher the mechanism of its formation using XRD. Radically two different ways, top-down and bottom-up approaches, have been employed to synthesize GQDs.[27,28] In top-down methods, GQDs are obtained from bulk carbonaceous materials, whereas in bottom-up techniques, carbon containing small molecular precursors are converted to GQDs.[28] Large precursor molecules often result in non-uniform emission;[29] hence, uniform size GQDs *via* a controlled synthesis are highly desirable. The solvothermal process is a bottom-up approach[26,27] for obtaining highly crystalline GQDs.[29] Compared to other quantum dots (QDs) and fluorescent dyes, GQDs have distinct advantages such as a relatively non-toxic nature and excitation dependent/independent fluorescence absorption.[6,9,26] Despite their appealing properties, the obtained GQDs usually require pretreatment[31] and surface passivation[13] giving a defective and polycrystalline structure showing poor optical properties. Subsequently, fast average photoluminiscence (PL) decay makes it difficult to detect them easily, restricting their wider application in biological imaging. Hence, doping GQDs with heteroatoms could efficiently tune the electronic density, band-gap and Fermi level, and improve the chemical activity and QYs of GQDs.[32–35] The light harvesting capacity of doped GQDs can be achieved through the quantum confinement effect and edge sites underpinned by their highly crystalline morphology which is correlated with optical performance.[26,35–38] Apart from the edge and electronic transition effect, mostly blue emission is reported for GQDs with a size ranging from 1.8 to 7 nm.[39] Furthermore, color emission can also be tailored by simply changing the reaction solvent or its pH.[36] The blue emission of the as-synthesized S-GQDs may be attributed to zig-zag edges.[21] Reduced cellular uptake and toxicity are typical stumbling blocks for carbon-based nanomaterials that curb the possibilities of their internalization inside living systems.[10] Biocompatibility is a key concept for understanding cell–biomaterial interactions,[6,40] so there is a need for the development of highly biocompatible luminescent GQDs, where conspicuous contrast images are desirable for tracking at the molecular level inside living systems.[4,41,42]

Herein, S-GQDs were obtained hydrothermally through a straightforward one-pot, rapid, and facile synthesis[43,44] using green second generation agro-industrial waste as a single source precursor, which is easily scalable and eco-friendly without the need for any catalysts or organic solvents. Conversely, in comparison with the multistep organic-phase reaction adopted by several groups, herein, a reproducible aqueous-phase process plays a pivotal role in an atom-economical,[27] simpler, gentle, and greener reaction. The employed precursor served as a low-cost and sustainable source of both carbon and sulphur resulting in a more accessible and high value-added product, *i.e.* S-GQDs. Sucrose and invert sugar are the major constituents of sugarcane molasses that serve as the carbon source.[45] Very impressively, a smaller carbon source leads to a narrow size distribution accelerating the narrow absorption and wide emission spectral characteristics leading to a higher quantum yield. Sulphur doping can effectively tailor the intrinsic properties of S-GQDs including their electronic and optical properties.[1,46,47] Waste molasses when subjected to hydrothermal synthesis also introduces a change in bandgap due to sulphur doping of ∼ 1.6%, which enhances the decay time for better detection. This leads to their improved biocompatibility, cellular distribution and light emission intensity resulting in a quicker response time and a wider dynamic range with a lower detection limit. Generally, carbene-like triplet ground states and doping effects are responsible for the photoluminescence (PL) phenomenon. The photoluminescence spectra of S-GQDs are normally broad and dependent on the excitation wavelength. In addition, the photoluminescence (PL) emission band also shifted from the visible to near infra-red region. The as-prepared S-GQDs display exceptional optical properties, such as wide and symmetric emission spectra with excitation wavelength-dependence/independence and three exponential lifetime decays, indicating their long average life of 3.1 ns. The as-synthesized S-GQDs from wastes achieved very high QY values ∼47%. Thus, the escalated nanophotonic and hydrophilic properties make S-GQDs imperative for high flux applications such as bioimaging, biosensing, diagnostics, and even drug delivery.[48] Furthermore, the obtained S-GQDs are nearly single crystalline

in appearance as they show a set of hexagonal spots with symmetry points in the selected area electron diffraction (SAED) pattern, demonstrating the well-ordered uniform growth of graphene nanodots.[49] Being at the heart of sustainable development, S-GQDs have extensively been explored for *in vitro* and *in vivo* imaging[50] due to their intrinsic fluorescence and characteristic planar surface for π–π interactions.

We further performed cyto-, hemo-, and histocompatibility assays to assess the biocompatibility of S-GQDs. Additionally, a functional observational battery (FOB) was used to detect the instant undesirable effects of S-GQDs on the behavioral and functional integrity of animals. A systematic comparison of the localization of S-GQDs was performed using different lineage systems such as primary chicken fibroblast DF-1 (normal cell line), human embryonic kidney (HEK-293) cells (normal human cell line), and human hepatocarcinoma (HepG2) cells. The results validated S-GQDs as a potential candidate for cancer cell bioimaging. Bright uniform blue micrographs of DF-1 provide insight into the high retention of S-GQDs at the cell surface without any significant cellular permeability followed by relatively more S-GQD cytoplasmic internalization for HEK-293 cells. Conversely, HepG2 cells treated with S-GQDs show an intense bright blue fluorescence using DAPI-FITC excitation and emission filters, suggesting significant probe retention in the cytoplasmic area.

These findings suggest low cost, robust, photostable, highly biocompatible, single crystalline, and water-processable fluorescent S-GQDs as well as their safe deployment in optical imaging, especially concerning the emerging need for a high-resolution bioimaging probe.

Experimental

Methods and materials

Agro-industrial waste molasses were procured from a sugar mill at Shamli, Uttar Pradesh, India. The *in vivo* and *in vitro* animal model experimental protocol for the present study was approved by Institutional Animal Ethics Committee (approval no: CPCSEA/AIP/2015/03/005), Amity Institute of Pharmacy, Amity University, Noida, Uttar Pradesh as per the guidelines of the Committee for the Purpose of Control and Supervision of Experiments on Animals under Chapter 4, Section 15(1) of the Prevention of Cruelty to Animals Act 1960 (CPCSEA); Ministry of Environment, Forest & Climate Change, Government of India, (Animal Welfare Division). Primary chicken fibroblast cells (DF-1) were obtained from 9 days old chicken embryo and cultured using Medox (cat. no. 1139), Bangalore, India, whereas human embryonic kidney (HEK293) and hepatic carcinoma (HepG2) cells were purchased from the National Centre for Cell Science (NCCS), Pune, Maharashtra, India. Quinine sulphate was purchased from Sigma Aldrich.

Synthesis of S-GQDs

S-GQDs were synthesized under mild hydrothermal conditions. Briefly, 5 ml precursor molasses was stirred for 2 h, sealed in a 40 ml PTFE-lined stainless steel autoclave and heated at 180 °C for 4 h under autogenous pressure. The resulting black colored crude product molasses cake (Mc) was washed with de-ionized water and filtered through several grade Gooch crucibles. Post filtration, Mf (molasses filtrate) was sonicated for 2 h and dried in a hot-air oven to get S-GQDs. By comparing the weight of Mc with that of Mf, it was estimated that the weight percentage of S-GQDs was about 20%. Optimization of the parameters for the synthesis was achieved by carrying out the synthesis at varying temperatures and time.

A Pt-electrode acquired from Gamry Instruments, USA, with a geometrical area of 0.071 cm^2 (3 mm in diameter) was used for sensor preparation. Prior to use, the Pt-electrode was polished with 0.1 μm, 0.3 μm and 0.5 μm of alumina/DI water slurries on a polishing cloth to obtain a mirror-like finish. The polished electrode was then rinsed thoroughly with ethanol solution, acetone solution, and DI water in an ultrasonic bath. Subsequently, the electrode was then sonicated in acetone and DI water, respectively. The electrode was then air dried under ambient conditions. 5 μl of the sonicated Mc was drop coated onto a conductive electrode surface (*e.g.* Pt-) and dried under ambient conditions. All voltammetric measurements were carried out in a three electrode cell using a Gamry Reference 600 Potentiostat/Galvanostat/ZRA where a Pt-wire was taken as the counter, an Ag/AgCl electrode as the reference and the Mc modified Pt-electrode as the working electrode.

Characterization

Morphology. The high-resolution X-ray diffraction (XRD) pattern was obtained using a PANalytical Empyrean X-ray diffractometer in the 2θ range of 10–60°. The PXRD pattern was recorded using CuKα radiation (1.5406 Å). X-rays were recorded with finely ground solid samples. Transmission electron microscopy (TEM) and high-resolution transmission electron microscopy (HRTEM) images were obtained on a JEOL, JEM-2100F electron microscope at an acceleration voltage of 200 kV. Samples were prepared by drop casting the material onto a carbon coated copper grid followed by drying at room temperature. Atomic force microscopy (AFM) images were obtained using a Nanoscope IIIa at IUAC (Inter University Accelerator Centre), New Delhi in tapping mode to see the morphology of the samples. AFM samples were prepared by spin-coating an aqueous solution of S-GQDs on silicon wafers. Sonication was performed using Telsonic Ultrasonics.

Chemical composition. Fourier transform infrared spectra were recorded using KBr pellets on a Nicolet-5DX FTIR spectrophotometer. The spectra were obtained from 400 to 4000 cm^{-1}. X-ray photoelectron spectroscopy (XPS) measurements were performed on a Kratos Axis Ultra Photoelectron Spectrometer which uses Al Kα (1253.6 eV) X-rays. Curve fitting and background subtraction were performed using Casa XPS version 2.2.73 software. Raman spectroscopy was performed on a confocal micro-Raman LabRam HR spectrometer (Horiba Scientific) by using backscattering geometry with a CCD detector and a 532 nm Ar laser and 100× magnification. Calibration

was initially done using an internal silicon reference at 520 cm^{-1} which gave a peak position resolution lower than 1 cm^{-1}. The energy dispersive analysis of X-rays (EDAX) was carried out on a Leica S4401 scanning electron microscope fitted with a Link Isis spectrometer.

Optical characterization of S-GQDs. A UV-Vis spectrum was recorded using a UV-1650 Shimadzu spectrometer. Photoluminescence (PL) measurements were performed using an FLS 920 peak Edinburgh analytical instrument apparatus with a xenon lamp as an excitation source. Excited-state fluorescence intensity decay data were acquired in the time domain using a Horiba Jobin Yvon Fluorocube time-correlated single photon counting (TCSPC) fluorimeter. The samples were excited at 340 nm using a UV-pulsed NanoLED-340 source having a pulse width <1.0 ns. The emission was collected using a Peltier-cooled red-sensitive TBX-04 PMT detection module at 425 nm and 450 nm. The data were collected with a DAQ-MCA-3 Series (P7882) multichannel analyzer. The excited-state fluorescence intensity decays were analyzed using DAS6 analysis software. Quantum yield (QY) measurements were made using quinine sulphate (QY ~ 54%) in 0.05 M H$_2$SO$_4$ as a reference sample and the QY of GQDs was calculated using the formula given in Table S1.†

***In vitro* cytotoxicity, hemocompatibility, and cell imaging.** *In vitro* cytotoxicity assay of S-GQDs was performed using primary chicken embryonic fibroblast cells (DF-1) from 9 days old chicken embryo (procured from Midnapore, West Bengal, India), human embryonic kidney cells HEK 293, and the human hepatic carcinoma cell line HepG2. The cells were cultured in Dulbecco's modified Eagle's medium (DMEM, HIMEDIA) supplemented with 10% fetal bovine serum (FBS) (HIMEDIA) and penicillin–streptomycin (penicillin: 100 U ml^{-1}, streptomycin: 100 mg ml^{-1}) and incubated at 37 °C with 5% CO$_2$ in a humidified atmosphere. 10^4 cells were taken in each well of a 12 well plate. 3-[4,5-Dimethylthiazol-2-yl]-2,5-diphenyltetrazolium bromide (MTT) assay was conducted as per J. Mosmann's method with modifications. Percentage viability was calculated as per the formula given in the ESI.† All experiments were carried out in biological triplicate. In order to elucidate the dose–response curve, concentration-dependent cellular cytotoxicity was analysed using S-GQDs with a concentration ranging from 200 μg ml^{-1} to 10 mg ml^{-1} and they were incubated for 24 h followed by cytotoxicity assay. The concentration was expressed in log and a graph was plotted between log concentrations *vs.* % viability. Time-dependent cellular cytotoxicity was analysed with 2 mg ml^{-1} of S-GQDs treated further for 48 and 72 h for assessing chronic toxicity.

For haemocompatibility, fresh as well as defibrinated blood was collected from healthy rats by a retro-orbital puncture using disposable syringes containing 4.9% citrate–phosphate–dextrose–adenine (CPDA) solution. The normal saline equilibrated sample was prepared with freshly isolated un-coagulated blood for the estimation of hemolysis. 100 μL from a prepared sample was incubated with 2 mg ml^{-1} S-GQDs at 37 °C for 2 h in a 5% CO$_2$ incubator at 95% humidity. The absorbance was measured at 540 nm which accounts for the total hemoglobin content in blood plasma, hence indicating the total concentration of lysis. Normal saline or 1% triton-X combination with a blood sample was considered as negative and positive controls, respectively. All the experiments were done in biological triplicate. Furthermore, freshly collected blood with 4.9% (CPDA) was centrifuged at 1500 RPM for 20 minutes. The collected pellet was re-suspended with normal saline (1 : 9 v/v). Subsequently, 100 ml of this solution was mixed again with 600 ml of normal saline. This final equilibrated sample was incubated with saline or 2 mg ml^{-1} S-GQDs at 37 °C for 2 h in a 5% CO$_2$ incubator at 95% humidity. After incubation, both saline and GQD treated cell suspensions were smeared on a glass slide and observed under a compound microscope at 100×.

HepG2 cells were seeded on sterile cover-slips in a 12-well plate at a concentration of 10^4 cells per well. S-GQDs (50 μg ml^{-1}) were added, and the cells were incubated at 37 °C at 5% CO$_2$. Fluorescence emission was observed from the cytoplasm within 4 h. Fluorescence micrographs revealed that only HepG2 cells treated with S-GQDs showed an intense bright blue fluorescence using DAPI-FITC filters.

Biochemical assay and histology. Healthy Wistar rats were treated with normal saline and S-GQDs (10 mg kg^{-1}, the *p.o.* and *i.p.* routes). Based on the allometric scaling approach, we have considered 10 mg kg^{-1} (*p.o.* and *i.p.* route) as the appropriate dose of S-GQDs for administration in Wistar rats. This method is a common strategy adopted to derive the maximum dose for animal studies.[51] SGOT/SGPT levels were examined in blood serum using an enzyme assay kit to find any detrimental effect of S-GQDs on liver function. Data were obtained spectrophotometrically (LABINDIA 3000, India) at 340 nm. Further organ toxicity was assessed on the heart, liver, kidneys, and brain for any structural changes by histological assessment of the respective organs. Cryo-sections of tissues were stained with H and E (haematoxylin and eosin) and mounted slides were observed at 100× magnification.

Results and discussion

Herein, we devised a simple, convenient catalyst- and template-free method for the gram scale production of single crystalline, highly fluorescent, water-processable S-GQDs using cheap bio-waste, *i.e.* sugarcane molasses, as the precursor *via* the green chemistry approach (Scheme 1). Hence, the use of molasses as a green carbon precursor through zero waste generation has been carving avenues towards sustainability, avoiding the laborious multi-step processes with hazardous agents and template preparation. As a proof of comprehensive synthesis, whole precursors transformed into valuable products, namely molasses filtrate (Mf) and molasses cake (Mc) without any waste products presenting huge economic and environmental advantages. A good balance of electrical conductivity and surface charges makes Mc a significant material for electrochemical sensing (Fig. S1†).
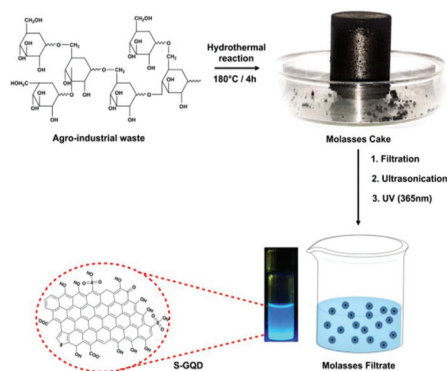
Scheme 1 Schematic illustration of the mass synthesis of S-GQDs from agro-industrial waste.

Cyclic voltammetry and electrochemical impedance spectroscopy (EIS) were performed to characterize the electrocatalytic biosensing abilities of the as-synthesized Mc, thereby assessing the performance of Mc as a sensor material. The Nyquist plot of Pt- and Pt-S-Mc exhibited a semicircle at higher frequencies and a marginally inclined line at lower frequencies. These observations establish that it is a diffusion controlled current process, accompanied by a limited charge transfer. Therefore, it was demonstrated that the modification of the bare Pt-electrode with Mc resulted in an enhancement in the electron transfer rate, further ameliorating the conductivity of the Pt-S-Mc working electrode (Fig. S2, ESI†).

The as-synthesized S-GQDs using the green hydrothermal method were also found to be conductive and highly stable in the aqueous phase and no precipitation was observed even after six months. However, at higher concentrations S-GQDs have a tendency to form aggregates,[2] whereas at a lower concentration, discrete S-GQDs are surrounded by a solvation shell[30] due to static charge (COO^-) on their surface making them a non-toxic material for cellular uptake. Additionally, under UV illumination (excitation 365 nm), the persistent and reproducible fluorescence of S-GQDs makes them suitable for bioimaging. The concentrated solution of S-GQDs exhibited less fluorescence intensity owing to its PL quenching, possibly due to the intermolecular interaction in comparison with the dilute solution.[2]

By employing a series of characterization methods such as X-ray diffraction (XRD), high resolution transmission electron microscopy (HRTEM), SAED, Fourier transform infrared (FTIR) spectroscopy, X-ray Photoelectron Spectroscopy (XPS), atomic force microscopy (AFM), Raman, and PL analysis, the intrinsic structural and morphological features of S-GQDs were revealed.

Morphological and structural properties of S-GQDs

For the first time, XRD analysis was employed chronologically to decipher the plausible mechanism of S-GQD formation from precursor molasses (Mp) *via* a hydrothermal route based on the changes in the amorphous and crystalline domains. The agro-industrial waste molasses was vacuum dried at room temperature and analyzed through XRD, which indicates (Fig. 1a) a combination of the major amorphous carbon phase with small crystalline domains. To confirm our hypothesis about the effect of temperature on the degree of crystallinity for the precursor material, XRD analysis of the oven-dried sample was also performed. Oven-dried molasses (Md) displayed a polycrystalline nature (Fig. 1a). The dominating peak was a cyclohexane monoclinic carbon phase (JCPDS file 48-1960) along with a cubic phase (JCPDS file 18-0311), graphene orthorhombic (JCPDS file 75-2330) and a small amount of graphene hexagonal (gH) (JCPDS file 75-1621) phase. After the hydrothermal treatment, the cyclohexane monoclinic carbon phase dramatically decreased with a concomitant increase and textured growth of the gH phase in the case of Mc. Possibly, the effect of temperature and autogenous pressure on hydrothermal carbonization results in crystal reorientation towards gH as the dominating phase (FWHM = 0.0059°). The amorphous phases were completely removed upon filtration using a different grade Gooch crucible. The PXRD pattern for Mf (Fig. 1b) illustrates three well-resolved scattering peaks at 28°, 41°, and 50°, associated with the (002), (101), and (004) planes, respectively, of 2D hexagonal reflections. Furthermore, a strong diffraction peak with high intensity at $2\theta = 28°$ having an inter-layered spacing of 0.33 nm predicts the absence of steric hindrance in the basal plane leading to their compact stacking, similar to that of bulk graphite. This favors the development of a graphene framework with almost no defects and a high degree of crystallinity during the carbonization process. An in-plane lattice spacing of 0.21 nm (101) as observed in XRD was consistent with that of the HRTEM images along with the SAED pattern (Fig. 2c and d).[12,17] Both the (002) interlayer spacing and (101) in-plane lattice spacing occur in GQDs; however, the former has been widely studied. Ultrasonication for ~2 h followed by drying resulted in the formation of high-quality S-GQDs having a low defect ratio and high crystallinity. The XRD pattern showed a broad and less intense peak of the (002) plane which shifts to a lower angle $2\theta = 25°$ demonstrating that the as-synthesized S-GQDs are of small size consisting of very few layers of graphene (Fig. 2b).

The HRTEM image of S-GQDs displayed well resolved lattice fringes with an average in-plane lattice spacing of 0.21 nm (Fig. 2a and b) for the (101) crystal plane of graphite,[52] further validating the layered structure of GQDs. The above results confirm that the graphitization happened during the synthesis of S-GQDs. SAED patterns and HRTEM images could be indexed to a perfect hexagonal pattern (Fig. 2b–d) of AB Bernal-stacked graphite[49] in the inner hexagon of 0.21 nm spacing, indicating a defect-free single crystal. The absence of extra sets of spots in the SAED patterns (Fig. 2c and d) shows that the domains are devoid of rotational stacking faults,[32] typically detected in turbostratic graphite.[49] The statistical analysis of the TEM image (Fig. 2a) gives a Gaussian size distribution (inset of Fig. 2a) with 3.5 ± 1.25 nm lateral size with a full width at half maximum (FWHM) of 2.9 nm confirming the uniform and homogeneously dispersed properties of our material. The uniform heating of molasses during the hydro-
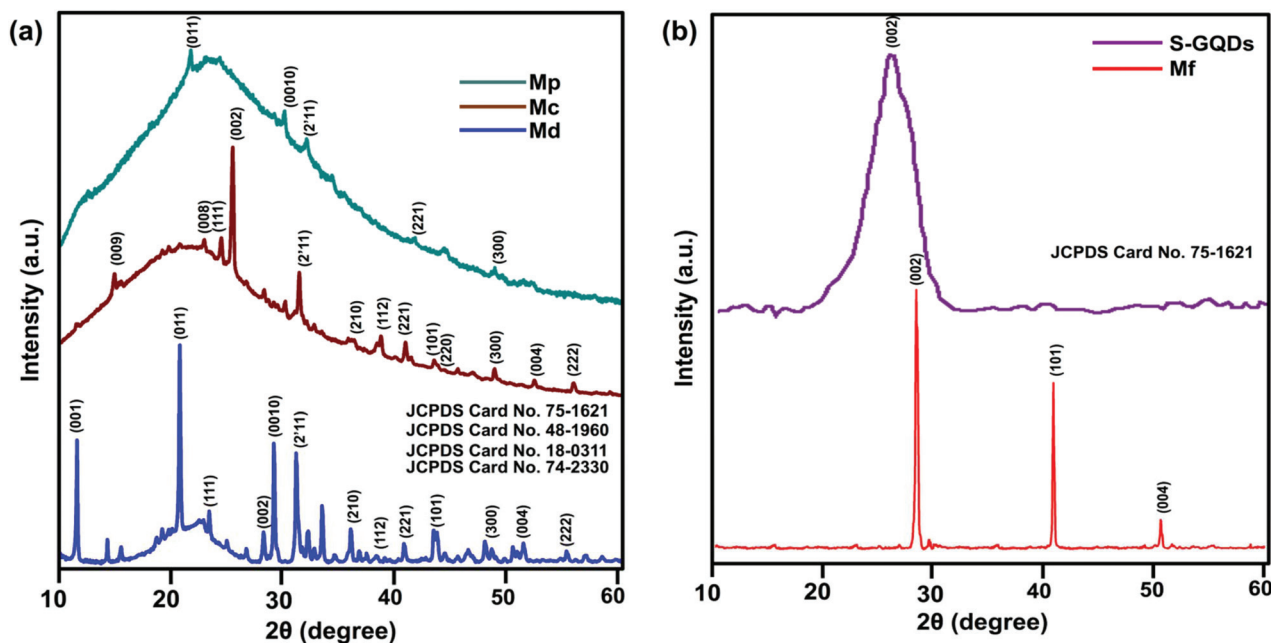
Fig. 1 Powder X-ray diffraction pattern. (a) Effect of temperature and pressure. Molasses precursor (Mp) as starting material, molasses cake (Mc) obtained after the hydrothermal reaction, and molasses oven-dried (Md) where the major phases are cyclohexane monoclinic [(011), (111), (2'11), (221), (112) (JCPDS file 48-1960)], graphene orthorhombic [(008), (0010) (JCPDS file 74-2330)], graphene hexagonal [(002), (101), (004) (JCPDS file 75-1621)] and cubic [(300), (220), (210), (200) (JCPDS file 18-0311)]. (b) S-GQDs obtained from the molasses filtrate (Mf) after ultrasonication where graphene hexagonal is the dominant phase.

thermal treatment was responsible for the regular nucleation and growth of S-GQDs[10] leading to their monodisperse property.[47,53]

The obtained S-GQDs were further characterized by tapping mode atomic force microscopy (AFM). The typical AFM images of S-GQDs were obtained in two different concentrations (Fig. 2e and f). Depending on the concentration, the S-GQDs have a tendency to self-assemble in an aqueous medium, forming 'self-assembled'[10] S-GQDs (Fig. 2f). These self-assembled S-GQDs are a kind of J-type aggregate, which were also observed in AFM (Fig. S3, ESI†) and HRTEM (Fig. S4, ESI†) images at a high concentration to be either overlapped or end-to-end stacked (head to tail arrangement) due to the π–π intermolecular interaction (Fig. 2f) proposing a brickwork model. Well-dispersed and homogeneous dots with a particle height distribution ranging from 0.9 to 1.1 nm and a topographic height of around 1 nm were observed in the very dilute sample (Fig. 2e). Three locations were arbitrarily chosen which presented an aggregate height of 3.5, 4 and 3 nm, respectively. Yields and the average height of 3.3 nm indicate the ~2–3 layers[36] of S-GQDs gathered end to end in the brickwork configuration shown in Fig. 2f which is in accord with numerous reports. The self-assembled J-aggregates were further confirmed with the photoluminescence characterization of S-GQDs. There is a red shift in absorption maxima with an increase in the concentration of S-GQDs giving rise to a new absorption in the range of 230–280 nm which is indicative of the self-assembled J-type aggregation.[54] In order to confirm the presence of dots, the AFM image of the pristine silica

surface (Fig. S3a, ESI†) as background and another phase image of the surface coated with S-GQDs were obtained (Fig. S3b, ESI†).

Composition of S-GQDs (FTIR, Raman and XPS)

To gain an insight into the hyperfine chemical structure, the FTIR spectra of S-GQDs and Mp were obtained (Fig. 3a). The changes in the functional groups of the product (S-GQDs) compared to Mp can be correlated from the characteristic FTIR peaks. Mp contains a high percentage of invert sugars which are linked with the help of glycosidic linkages. During hydrothermal carbonization, some of these linkages are broken, giving rise to freely exposed (–OH) groups, which are involved in intermolecular hydrogen bonding in aqueous medium providing a high solubility to S-GQDs and making them suitable for numerous applications in bio-systems. The broad peak at 3299.6 cm^{-1} was observed in the Mp which was attributed to the O–H stretching vibration.

Post hydrothermal treatment the O–H stretching peak becomes broader and split at ~3340 cm^{-1} and ~3262 cm^{-1} signifying the presence of chemically distinct alcoholic/phenolic groups in the molecule with differences in bond strengths and force constants. A new peak at around 1412 cm^{-1} appeared in the spectra of S-GQDs indicative of the –OH bending vibration. The content of 'H' was drastically decreased in the S-GQDs which was reflected in the weakened vibration peaks at ~991 cm^{-1} (C–H bending) and 2930 cm^{-1} (C–H stretch of the methylene group) compared to Mp. However, the newly emer-
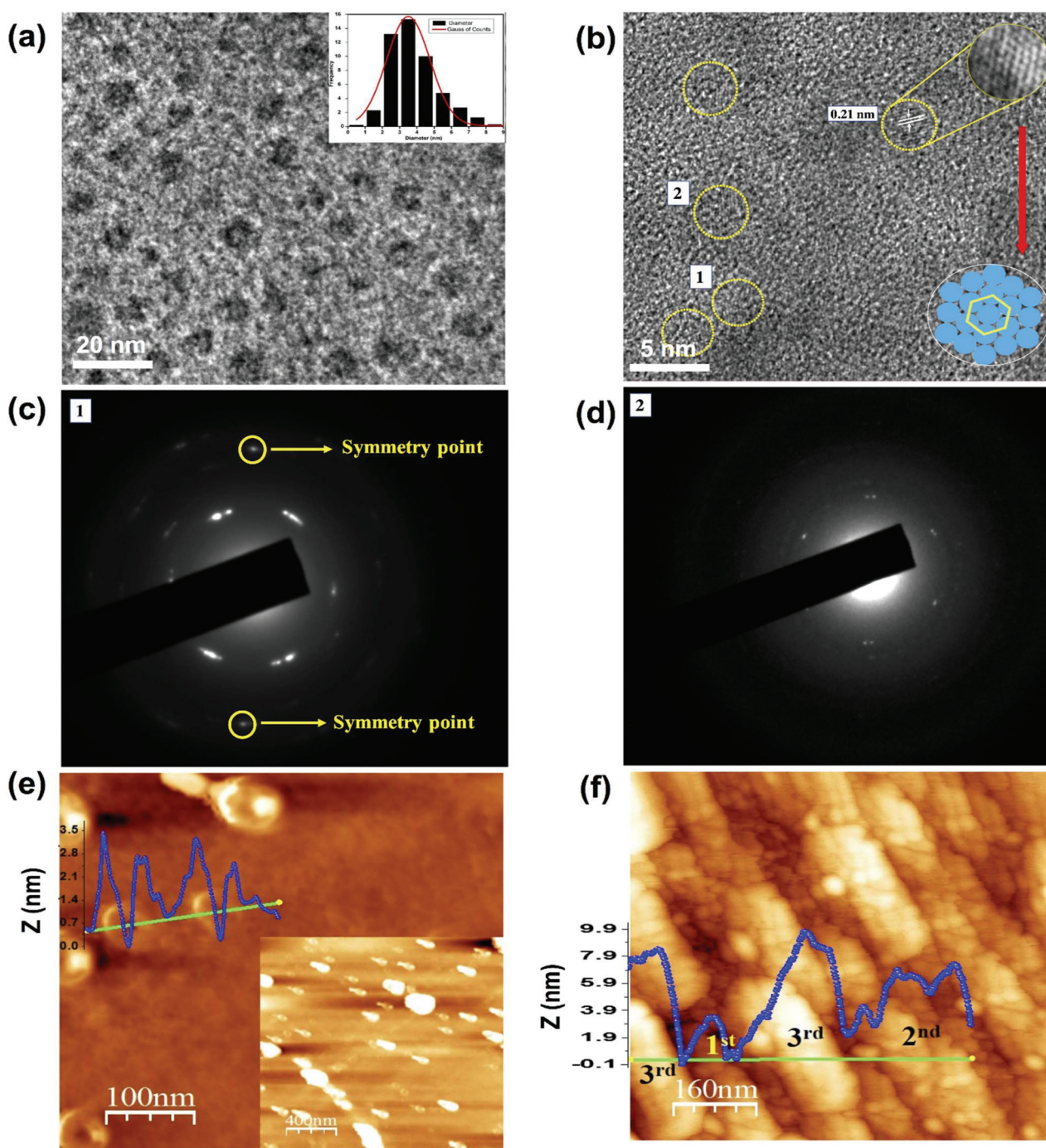
Fig. 2 Morphological characterization of S-GQDs. (a) TEM image (inset: lateral size distribution); (b) HRTEM image; (c) SAED pattern corresponding to area (1) in image (b); (d) SAED pattern corresponding to area (2) in image (b); AFM image observed at (e) lower concentration; (f) higher concentration with a height distribution profile.

ging peaks at ~1041 and ~780 cm^{-1} in the spectra of S-GQDs confirm the effective doping of sulphur into the carbon matrix after the hydrothermal reaction. Furthermore, the presence of sulfur was also confirmed through the EDAX spectrum of Mf (Fig. S5†) (Table S2†). Moreover, the characteristic conjugate peaks at ~1311 cm^{-1} and ~1117 cm^{-1} arise from the asymmetric and symmetric SO$_2$ stretching, respectively. Peaks at

~1041 cm^{-1} and ~780 cm^{-1} in the spectra of S-GQDs were attributed to the thiocarbonyl bending and C–S stretching vibrations, respectively. The peaks centered at around ~1600 cm^{-1} and ~1400 cm^{-1} are attributed to the asymmetric and symmetric stretching of COO$^-$ of the organic acid in Mp. The COO$^-$ stretching due to the presence of acidic groups in the Mp is in good agreement with earlier reports.[46] The dis-
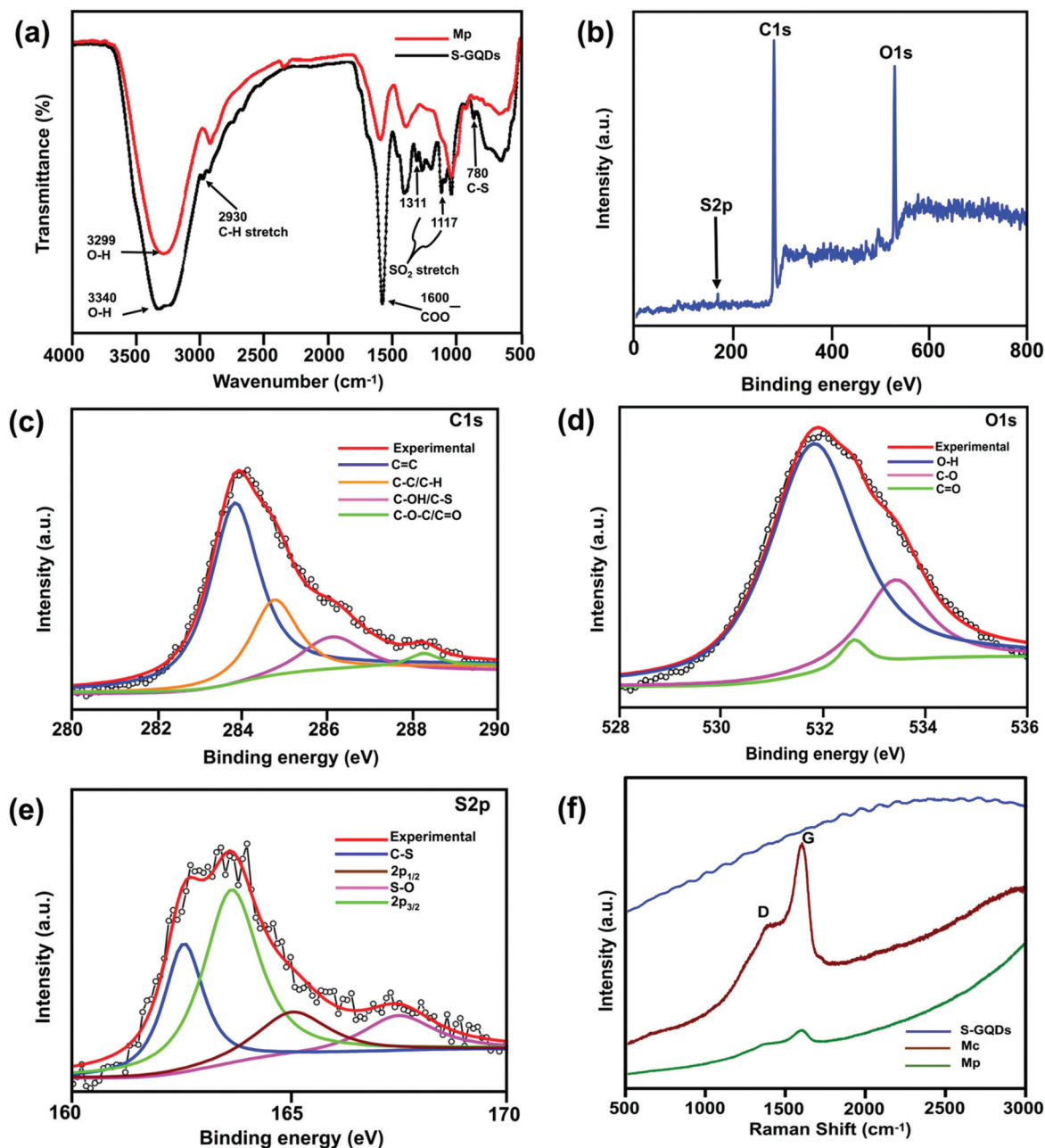
Fig. 3 Structural characteristics of S-GQDs. (a) FTIR spectrum; (b) survey XPS spectrum; (c) high resolution C 1s spectrum; (d) high resolution O 1s spectrum; (e) high resolution S 2p spectrum; (f) Raman spectrum.

appearance of these peaks with the appearance of a highly intensified peak at 1585 cm^{-1} in S-GQDs confirms the presence of the C=C stretching mode of polycyclic aromatic hydrocarbons in S-GQDs.

S-GQDs showed high performance in optoelectronic properties, hence it is essential to study the chemical bonding states of these S-GQDs. XPS measurements were performed to investigate the composition as well as the quantitative analysis of the as-synthesized S-GQDs (Fig. 3b). The dominant binding energy peaks at 284 eV and 532.2 eV are attributed to the presence of C 1s and O 1s electrons which are the key elements of

S-GQDs. However, in S-GQDs, an extra peak was observed at 167.4 eV, which is ascribed to the S 2p electrons. The carbon, oxygen, and sulphur atom configurations in S-GQDs were analyzed by the deconvolution of C 1s, O 1s, and S 2p peaks into four, three and four Gaussian parts, respectively. The C 1s spectrum can be deconvoluted into one large and three small peaks, centred at 283.8 eV (large peak for C=C), 284.5 eV (C–C, C–H), 286.1 eV (C–OH, C–S, C–O–C), and 288.4 eV (COOH, C=O) (Fig. 3c). The C=C component is the main carbon bonding configuration having the most intense peak among all the deconvoluted peaks, which means that the as-

prepared S-GQDs have an abundant graphitic matrix structure. The peak at 286.1 eV is assigned to the C–OH bonding as S-GQDs have a high density of hydroxyl groups on the surface responsible for hydrophilicity. The O 1s spectrum (Fig. 3d) of S-GQDs is composed of three peaks centered at 531.8 eV, 532.6 eV, and 533.5 eV, suggesting that oxygen exists in three different forms O–H, C=O/COOH, and C–O, respectively. The maximum intensity of O–H among all peaks of O 1s suggests that the hydroxyl group is more exposed at the edge sites of S-GQDs rather than at the basal plane sites generating a defect-free structure which is also reported by other groups.[55,56] In Fig. 3e, the S 2p spectra of S-GQDs supported the formation of the C–S bonding. However, the weak intensity of the C–S bonding in S-GQDs at 286.1 eV confirmed the presence of a very small amount of sulphur in S-GQDs. The low intensity peak located at 167.5 eV in the S 2p spectrum of S-GQDs is attributed to oxide sulphur. The C–S bond generated at 162.5 eV with the second highest intensity peak indicates the presence of sulfur in S-GQDs. The remaining peaks centred at 165.1 eV and 163.6 eV are $2p_{1/2}$ and $2p_{3/2}$, respectively, of the thiophene like-S peak due to spin–orbit coupling.[33] Therefore, doped sulphur in S-GQDs exists in three configurations: oxide sulphur, C–S and thiophene sulphur (Fig. 3e).[16]

Raman spectroscopy, a non-destructive technique,[28] was used to investigate qualitatively and quantitatively the degree of structural disorder in the carbon matrix, based on different types of defects such as grain boundaries, point defects, stress, strain, stacking faults, edges, doping, vacancies, functional groups etc.[57] Herein, we have systematically probed the intri-

guing conversion of S-GQDs and black Mc from Mp as a function of both temperature and pressure using Raman spectroscopy.

Generally, the intensity ratio of D and G bands (I_D/I_G) is used to decipher the structural order between amorphous and crystalline graphitic systems.[28] (Fig. 3f) After hydrothermal carbonization, the intensity of the D to G peak I_D/I_G decreases abruptly from 0.89 to 0.64 for Mp to Mc implying a significant increase in the size of in-plane sp^2 domains and a decrease in disorderliness. The increase in G-band can be attributed to the long range ordering.[57] The intensity ratio further indicates the graphitic order in the product after hydrothermal treatment depicting its high crystallinity as supported by XRD and HRTEM. However, in this report the D- and G-bands for the as-synthesized S-GQDs were not very conspicuous as the Raman signals of strong fluorescent S-GQDs were concealed by the intense fluorescence in the background.[58]

Optical characterization of S-GQDs

The optical properties of S-GQDs were studied using UV-Vis absorption spectroscopy and PL spectroscopy. Mostly GQDs have an absorbance band in the UV region between 260 and 320 nm assigned to the π–π* transition of the C=C bonds with sp^2 hybridization and, sometimes, a weaker shoulder at 270–400 nm attributed to the n–π* transitions of the C=O bonds, with a tail extending into the visible wavelengths.[5,59–61] The UV-Vis spectrum exhibited typical absorption peaks at ~270 nm and a shoulder above 300 nm, attributed to the π → π* and n → π* transition of C=C bonds and C=O, respectively (Fig. 4a). The former absorption peak implied that
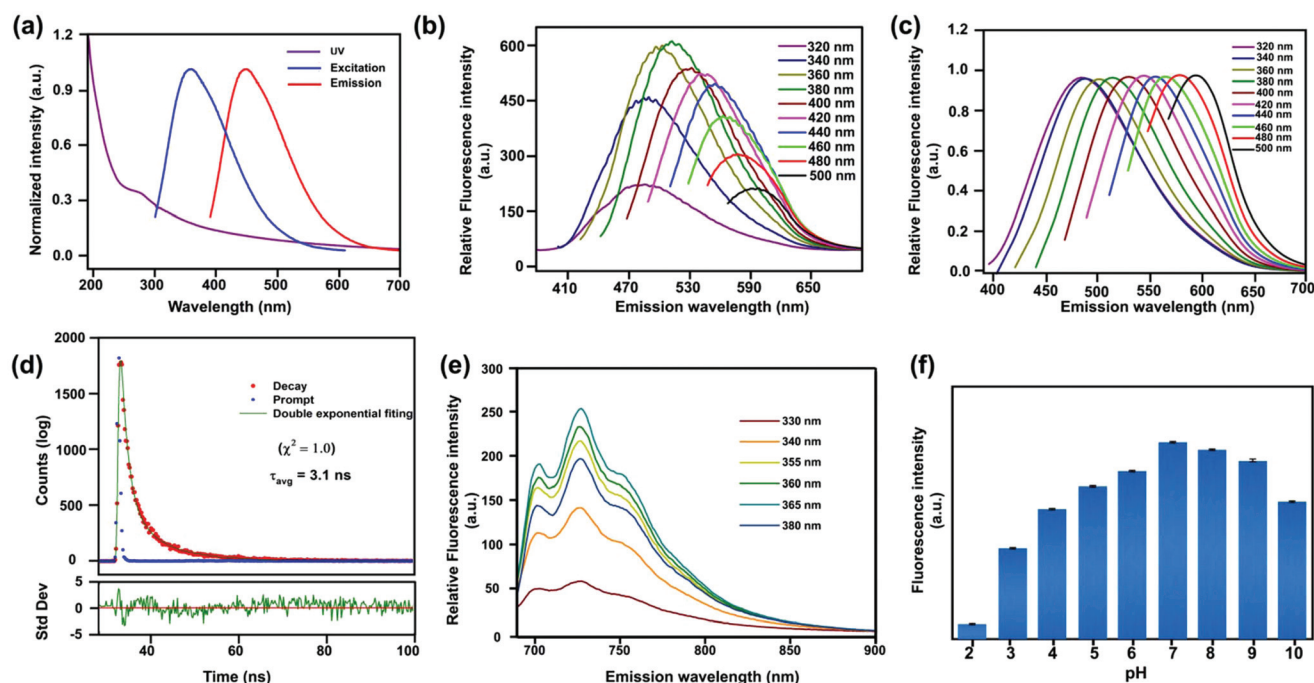

Fig. 4 Optical properties of S-GQDs, (a–d) in water. (a) UV-Visible absorption, fluorescence excitation and emission spectra; (b) PL spectra under excitation of different wavelengths; (c) normalized spectra of graph (b); (d) time resolved PL spectrum; (e) excitation independent fluorescent emission spectra of S-GQDs in acetone; (f) dependence of PL intensity on different pH values.

the electronic transition of aromatic sp^2 domains leads to the formation of delocalized π states on the basal planes which is similar to graphene. The n → π* transition of the carbonyl or carboxylic groups connected to S-GQDs produces PL emission at 436 nm beside the conjugated basal carbon skeleton. The broadband emission is attributed to the layered structure of S-GQDs which consists of a large conjugated system containing extensive delocalized π electrons. The obtained S-GQDs presented a wide spectral region and the emission covers the visible wavelength range extending to near-infrared, serving as a better light capturing medium for nano-photonics including bioimaging. Generally GQDs display photoluminescence emissions, which make them helpful for fluorescence bioimaging.[62] The emission spectra of the GQDs are dependent on the excitation wavelength. The shift in emission peak positions with different excitation wavelengths depends on several key factors such as the quantum confinement effect, size effects, elemental composition, edge states, surface functional groups, conjugated π-domains and defects in the carbon framework.[5,63] This can lead to different emissive trap sites and electron densities on the GQD surface affecting the PL properties, hence at particular excitation wavelengths some corresponding emissive trap sites would be excited, making GQDs emit that light. These results are in good agreement with earlier reports[5,62,63] which is clearly depicted in Fig. 4a. Depending on the nature of solvent, S-GQDs possess both excitation-dependent/independent fluorescence properties. Solvent-dependent fluorescence emission behaviour may also be attributed to solvation dynamics.[64] Unlike the fluorescence emission of conventional fluorophores such as organic dyes and inorganic quantum dots, the fluorescence emission of S-GQDs in water was found to be dependent on the excitation wavelength (Fig. 4b and c). However, excitation independent emission (Fig. 4e) was observed in the less polar solvent acetone confirming its defect-free structure.[65] Hence, our proposed simplified synthetic strategy helped in overcoming the limitations of a lower quantum yield of S-GQDs obtained in aqueous phase synthesis. The emission spectra for S-GQDs were obtained under excitation in the range of 320 to 500 nm with an increment of 20 nm. Interestingly, excitation at 320 and 500 nm resulted in an emission at 474 and 590 nm, respectively, as shown in Fig. 4b and c. Furthermore, the value of the Stokes shift decreased from 154 nm to 90 nm as the excitation changed from 320 nm to 500 nm (Fig. 4b and c), respectively. The emission peak maximum was obtained at 515 nm under excitation at 380 nm among all the excitations which displayed a red-shift towards 590 nm under the excitation at 500 nm.

Lifetime evolution of S-GQDs was investigated using steady state and time resolved PL measurements. The excited-state intensity decay data for S-GQDs dissolved in water were collected at 425 nm and 450 nm, by using a 340 NanoLED as the excitation source. The decay curves of S-GQDs can be fitted with double exponential function giving an averaged lifetime (τ_{avg}) of 3.1 ns. However, most of the literature used the double and/or triple exponential function to fit the decay curve of GQDs.

The results obtained for S-GQDs were explored in a similar way by fitting the excited state intensity decay data into the three exponential decay model and the parameters were recovered accordingly, along with the goodness-of-the-fit (χ^2) (Table S3†). In the three exponential decay model, the average lifetime consists of a fast component $\tau_1 = 0.28–0.42$ ns and two slow components ($\tau_2 = 2.47–2.71$ ns and $\tau_3 = 8.57–8.95$ ns) which complies with a previous report on the lifetimes obtained for doped GQDs,[31,47] where slower components correlate with the minor elements S and O (Fig. 4d). Moreover, the slow and fast component decay corresponds to the recombination from the intrinsic state quantum size and zigzag edge sites.[15] Furthermore, the photoluminescence of S-GQDs is stable with respect to photoirradiation for several hours, exhibiting no meaningful reduction in the observed intensities for the experiments with continuously repeating excitations. The as-synthesized S-GQDs achieved a high QY of 47% (Table S1†) with a longer decay lifetime (Table S3†) and further can be explored as nano-probes for live cell imaging.[6] S-GQD behaviour in other solvent media is under investigation in our laboratory. To further study the pH-dependent behavior of S-GQDs, we considered acidic (pH 3), neutral (pH 7) and alkaline (pH 10) media. The stable performance of PL was the highest at neutral pH compared to alkaline and acidic pH (Fig. 4f). Possibly, S-GQDs get highly protonated in acidic medium generating a carbene-like triplet state resulting in PL quenching. Interestingly, PL can be restored by changing the pH again, paving a way for turn-on/off sensors.

Highly fluorescent S-GQDs for improved bioimaging

Interconnected windows of the optical properties of S-GQDs with high QY and bioimaging[2] are a crucial goal, which poses a big challenge in the diagnostic arena. With superior optical properties and high photostability, the S-GQDs successfully overcame these challenges confirming their high *in vivo* biocompatibility and helped to navigate in the needed direction. A system should be cyto-, hemo- and histocompatible to account for biocompatibility. Herein, different lineage groups were considered for a comprehensive study to observe the effect of S-GQDs on cellular internalization: DF-1 cells for their susceptibility and response under mild stress conditions, HepG2 cells for their malignancy and high permeability and HEK293 cells were chosen as a model to quantitatively evaluate the differential fluorescence intensity of S-GQDs. To evaluate the primary cytocompatibility, concentration and time-dependent MTT assay was carried out with DF-1, HEK293, and HepG2 cells at different concentrations of S-GQDs ranging from 200 μg ml^{-1} to 10 mg ml^{-1} for 24 h as shown in Fig. 5a. Significant cell viability was observed with DF-1 (92%), HEK293 (95%), and HepG2 cells (88%) with 2 mg ml^{-1} of S-GQDs (Fig. 5a). Hence, this concentration was considered for further time-dependent and dose–response study to assess chronic toxicity. The results showed mild toxicity at 24 h of incubation for DF-1, HepG2, and HEK293 cells; however, cell viability was observed compared to the control after 72 h (Fig. 5b). To demonstrate their potential as a highly biocompa-
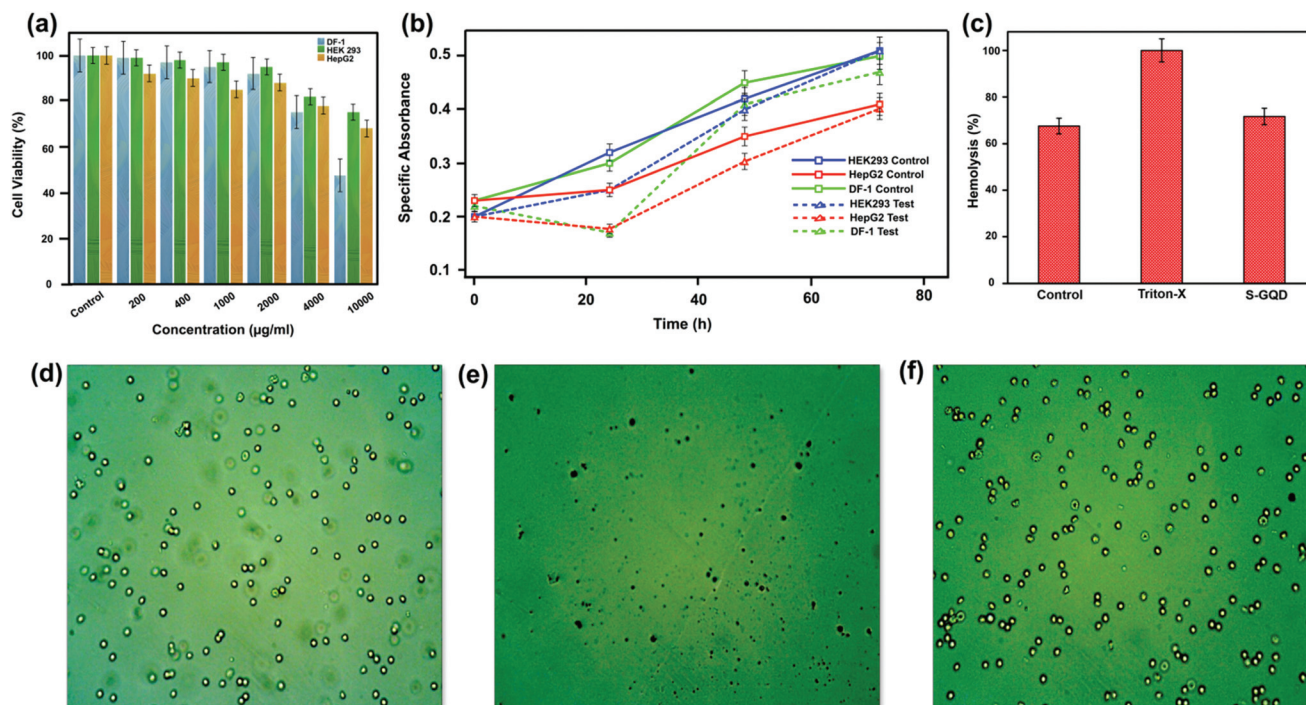
Fig. 5 Cytotoxicity assessment of S-GQDs with DF-1, HEK293 and HepG2 cells, (a) concentration-dependent cell cytotoxicity; (b) time-dependent cytotoxicity after 72 h of incubation; (c) hemolysis assay of RBCs; (d–f) RBC aggregation assay, (d) with saline, (e) with Triton X, (f) with S-GQDs.

tible material, hemocompatibility was investigated by performing an *in vitro* hemolysis assay (Fig. 5c). The material was found to be hemocompatible as it showed a lower RBC hemolysis rate compared to the threshold limit of 5%.

RBC hemolysis was evaluated after the addition of S-GQDs in defibrinated as well as fresh blood cells obtained from Wistar rats by retro-orbital puncture against the positive control (TritonX with blood) and the negative control (saline with blood). There were no significant changes in the percentage of RBCs for the test groups after 1 h of incubation when compared to the negative control. The hemolytic ratio of 1.03% suggested that our material is highly hemocompatible. Incubation of RBCs with S-GQDs revealed insignificant agglutination after incubation for 2 h (Fig. 5d–f) which further confirmed the hemocompatibility of our material.

For long-term retention studies,[66,72] loading was performed to assess the extent of intracellular localization of the as-synthesized fluorescent S-GQDs with DF-1 (Fig. S6, ESI†), HEK293 and HepG2 cells (Fig. 6) for a period of 4 h for bioimaging. Both self-assembled and solvated S-GQDs (typically smaller than 50 nm) have a self-localizing property and allowed effective cellular internalization selectively.[10,11] Image processing[67,68] (Fig. S7, ESI†) of the fluorescence micrographs of HepG2 cells revealed a fluorescence signal from the cytoplasm implying the abundant cellular uptake of S-GQDs at a concentration of 50 µg ml^{-1} (Fig. S8, ESI†). These images further confirm the significant probe internalization and augmented retention in HepG2 cells proving the utility of these water-soluble S-GQDs for cancer cell imaging (Fig. 6f–h), whereas for

DF-1 cells, fluorescence was mainly localized in the interstitium and circumjacent area of the cell (Fig. S9, ESI†).

HEK293 cells demonstrated a typical amoeboid shape with particle aggregates attached to the extracellular face of the plasma membrane, mainly in zones with abundant filopodia. However, no morphological abnormalities have been observed. Fluorescence micrographs (Fig. S8, ESI†) revealed that only HepG2 cells treated with S-GQDs show an intense bright blue fluorescence using DAPI-FITC excitation and emission filters. These bandpass filters provide the brightest possible images separating emission signals with minimum crossover interference while preventing unwanted light from reaching the detector.[69]

There are a handful of reports on the cellular uptake of graphene-based nanomaterials *via* energy-dependent pathways which primarily include clathrin-mediated endocytosis, caveolae/lipid-raft mediated endocytosis, and macropinocytosis.[8,70–72] The differences in the cellular permeation of nanomaterials are governed by various factors such as the cell type, the nature of nanomaterials, and the structure of cell membranes.[70–72] Considering their small size and better biocompatibility, GQDs are most likely to be internalized into cells *via* endocytosis.[8,70] Although caveolae are abundant structures on the plasma membrane,[73] their expression is stage and microenvironment dependent.[74] Possibly, early stage and premature cellular organization of DF-1 leads to underdeveloped caveolar structures, thereby resulting in poor uptake of S-GQDs.

In contrast, HepG2 cells are unable to endocytose nanoparticles by caveolae-mediated endocytosis due to a lack of
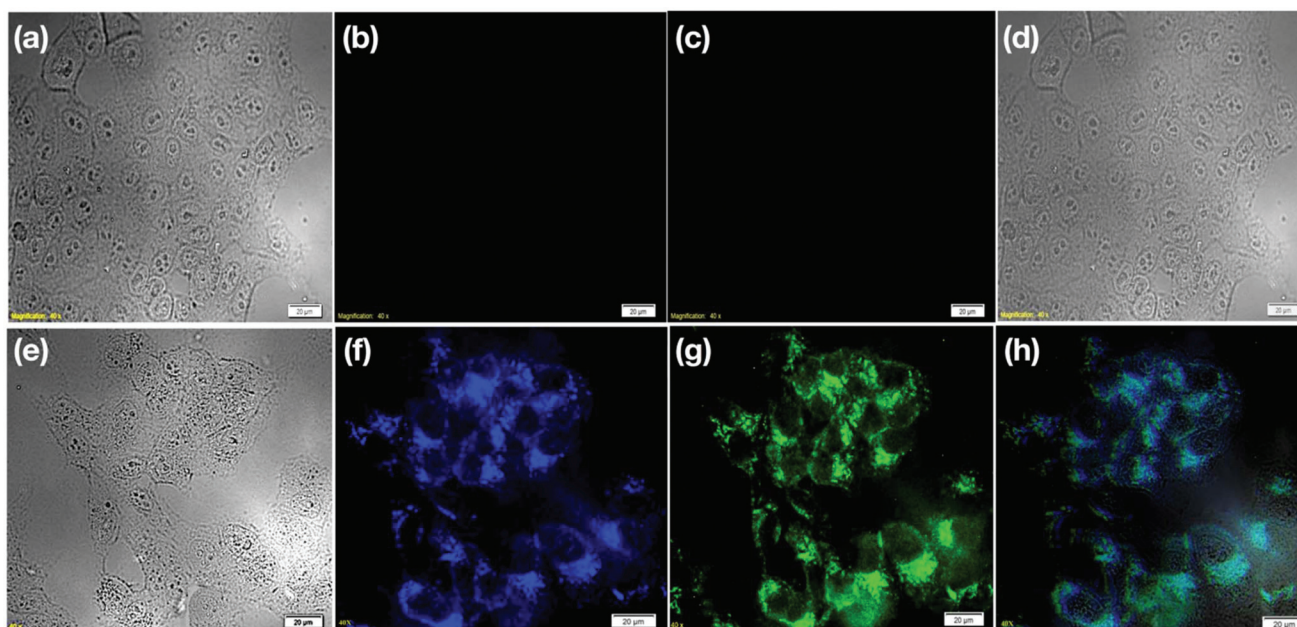
Fig. 6 Cell imaging. (a–d) DIC image of HepG2 without S-GQDs, (a) bright field (b) image at 405 nm excitation (c), image at 478 nm excitation and (d) merged image of (a–c); (e–g) DIC image of HepG2 using S-GQDs, (e) bright field, (f) image at 405 nm excitation, (c) image at 478 nm excitation, and (h) merged image of (e–g) at 478 nm excitation.

endogenous caveolin-1.[70–72] In the line of early reports, actin dependent macropinocytosis[70] forms a gateway for the internalization of S-GQDs, where the nanoparticles are encapsulated in an extracellular fluid forming macropinosomes through a nonspecific cellular uptake process.

However, due to the enhanced permeation and retention (EPR) effect,[75] the loss of occludin delineated tight junctions in HepG2 cell[76] delivery of S-GQDs may follow an alternative pathway. This mimics the microtubule-dependent uptake route, as was depicted by the stable fluorescence from the cytoplasm within 4 h without any external capping. Conversely, the tight junction[77] barrier present in the apical membrane of DF-1 and HEK293 cells is significantly protective against the internalization of S-GQDs thus confining fluorescence at the plasmalemma periphery (Fig. 7). The structure and functions of caveolae in the context of HepG2 cells is still a matter of debate, as their precise function is elusive. Our group is exploring in this direction to get further insight into the internalization of S-GQDs in these cells. The results of FOB confirmed no instant behavioral abnormalities with various parameters (Tables S4 and S5†). Furthermore, to evaluate biocompatibility, *in vivo* experiments were conducted to understand the physiological changes with S-GQDs treatment, if any.

Three animal groups were used to determine the *in vivo* biocompatibility having normal saline and S-GQDs treatment by the different routes of administration *i.e.* intraperitoneal and oral, respectively, for a period of 90 days. Furthermore, rats were sacrificed after 90 days and sections of vital organs were prepared for histological assessment. However, no apparent histological abnormality or lesions were observed. The central
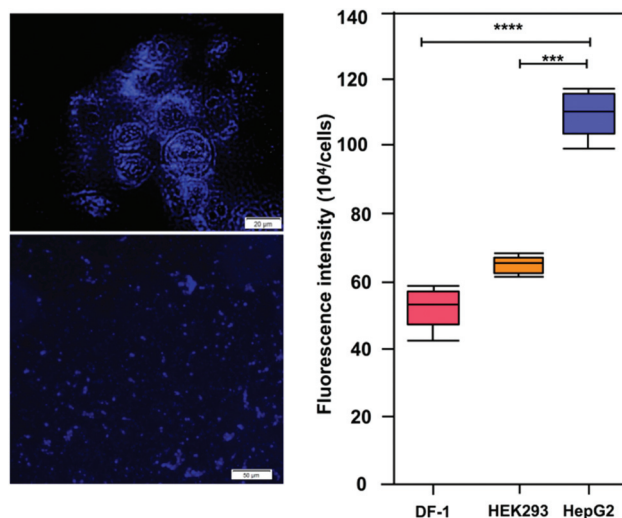

Fig. 7 Analysis of fluorescence intensity. DIC image after S-GQDs treatment at 405 nm (a) HepG2 cells, (b) DF-1 cells, (c) quantitative analysis of fluorescence intensity from DF-1, HEK293, and HepG2 cells. The figure is representative of multifocal observations of the separate images analysed.

vein and hepatocytes were found to be normal in all groups, without any indication of inflammatory response. Screening of SGOT/SGPT (Fig. S10, ESI†) markers again established functional normality by exposure of S-GQDs compared to the control. Similarly, a histological micrograph of the brain hippocampus region was observed to be normal. Clearance of
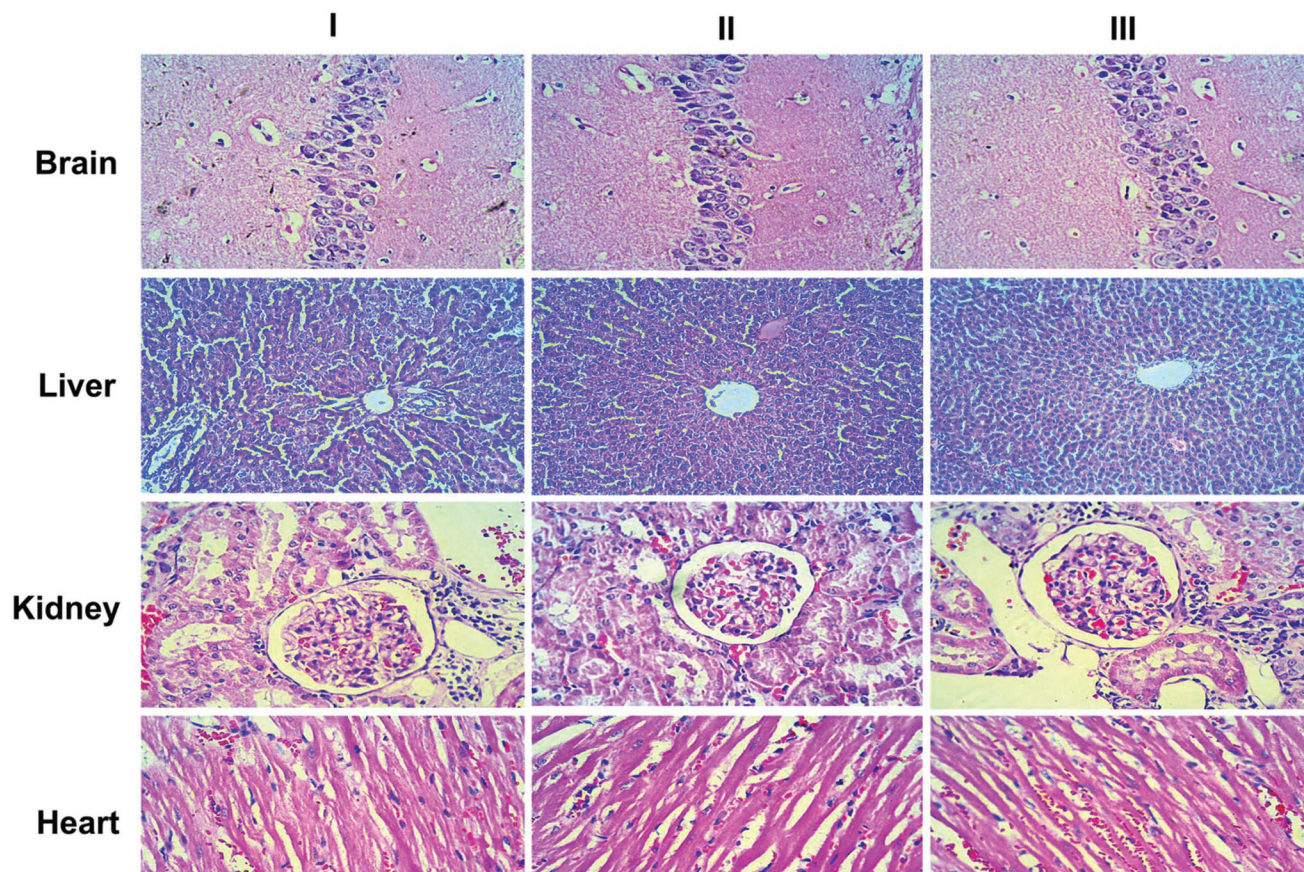
Fig. 8 Histological assessment of vital organs after 90 days of S-GQDs administration in Wistar rats. Hemotoxylin and eosin staining photomicrographs of the brain (hippocampal region), liver (central vein), heart (cardiomyocytes), and renal (glomeruli) in the control (panel I), intraperitoneal (panel II), and oral (panel III) at 40×.

blood vessels without necrosis of renal cells and tubular degeneration was observed in kidney sections. Normal renal parenchyma, tubules, and glomeruli were obtained from each group. Myocardial histological sections showed insignificant changes in test groups compared to the control group. No damage to myocyte nuclei and myofibrillar necrosis or vacuolization was noticed.

Blood vessels and myofibrils were normal in each group which proves S-GQDs as a highly biocompatible material (Fig. 8). These data indicate that S-GQDs may be applied for selective transport to hyper-permeable cells like hepatic cancer cells for selective fluorescence detection of cancerous cells at early tumor sites.

Conclusions

Our results are promising to utilise wastes (as well as energy) striving to encourage sustainability and concomitantly minimizing environmental burden.

In this study, we synthesized single crystalline S-GQDs from the agro-industrial waste sugarcane molasses *via* a hydrothermal route approaching towards a facile, one-pot, one-step, scalable, template- and catalyst-free, and green method. Here,

we demonstrated the exceptional ability of S-GQDs to label mainly the cytoplasmic area of HepG2 cells *in vitro* with minimal uptake by normal DF-1 and HEK 293 cells with concurrent differences in terms of photoluminescence and bioimaging characteristics. The experimental results confirmed that the 'blue-sky' S-GQDs with unique benefits of high crystallinity, water solubility, stability, excellent fluorescence, and biocompatibility can be specifically used for targeted theranostic applications. Furthermore, the pH-responsive fluorescence property of S-GQDs could be explored for scalable pH on/off sensors.

In the future, S-GQDs could be explored for simultaneous tracking at trans-cellular levels through selective bioconjugation to unravel the underlying molecular bio-dynamics. Our group is working in the direction of bio-orthogonal click chemistry for specific tagging of biological molecules for advanced labelling applications.

Author contributions

Sujata Sangam, Monalisa Mukherjee, Apoorv Gupta, and Rohan Bhattacharya wrote the main manuscript text and pre-

pared the figures. Apoorv Gupta, Adeeba Shakeel, Arun Kumar Sharma, Satendra Kumar Rajput and Biswarup Basu carried out the entire biological studies. Deepa Suhag, Sandip Chakrabarti, Sourav Chattopadhyay, and Sandeep Kumar Garg were involved in the CV, EIS, XPS, XRD and AFM analysis. Malay Kishore Dutta carried out the image processing study. Vinod Kumar was involved in the PL analysis. All authors have given their approval to the final version of the manuscript.

Conflicts of interest

There are no conflicts to declare.

Acknowledgements

References

1 H. Zhao, R. Ding, X. Zhao, Y. Li, L. Qu, H. Pei, L. Yildirimer, Z. Wu and W. Zhang, *Drug Discovery Today*, 2017, **22**, 1302.

2 R. Ye, C. Xiang, J. Lin, Z. Peng, K. Huang, Z. Yan, N. Cook, E. Samuel, C. Hwang, G. Ruan, G. Ceriotti, A. Raji, A. Martí and J. Tour, *Nat. Commun.*, 2013, **4**, 2943.

3 M. Bacon, S. Bradley and T. Nann, *Part. Part. Syst. Charact.*, 2013, **31**, 415.

4 Z. Fan, S. Li, F. Yuan and L. Fan, *RSC Adv.*, 2015, **5**, 19773.

5 T. Gao, X. Wang, L. Yang, H. He, X. Ba, J. Zhao, F. Jiang and Y. Liu, *ACS Appl. Mater. Interfaces*, 2017, **9**, 24846.

6 K. Habiba, V. Makarov, J. Avalos, M. Guinel, B. Weiner and G. Morell, *Carbon*, 2013, **64**, 341.

7 D. Iannazzo, I. Ziccarelli and A. Pistone, *J. Mater. Chem. B*, 2017, **5**, 6471.

8 C. Kinnear, T. Moore, L. Rodriguez-Lorenzo, B. Rothen-Rutishauser and A. Petri-Fink, *Chem. Rev.*, 2017, **117**, 11476.

9 A. Geim and K. Novoselov, *Nat. Mater.*, 2007, **6**, 183.

10 M. Kumawat, M. Thakur, R. Gurung and R. Srivastava, *Sci. Rep.*, 2017, 7, 1.

11 M. Kumawat, M. Thakur, R. Gurung and R. Srivastava, *ACS Sustainable Chem. Eng.*, 2017, **5**, 1382.

12 S. Baker and G. Baker, *Angew. Chem., Int. Ed.*, 2010, **49**, 6726.

13 S. Cheng, T. Weng, M. Lu, W. Tan, J. Chen and Y. Chen, *Sci. Rep.*, 2013, **3**, 2694.

14 S. Kim, S. Hwang, M. Kim, D. Shin, D. Shin, C. Kim, S. Yang, J. Park, E. Hwang, S. Choi, G. Ko, S. Sim, C. Sone, H. Choi, S. Bae and B. Hong, *ACS Nano*, 2012, **6**, 8203.

15 F. Zhang, F. Liu, C. Wang, X. Xin, J. Liu, S. Guo and J. Zhang, *ACS Appl. Mater. Interfaces*, 2016, **8**, 2104.

16 X. Li, S. Lau, L. Tang, R. Ji and P. Yang, *Nanoscale*, 2014, **6**, 5323.

17 R. Liu, D. Wu, X. Feng and K. Müllen, *J. Am. Chem. Soc.*, 2011, **133**, 15221.

18 N. Li, A. Than, X. Wang, S. Xu, L. Sun, H. Duan, C. Xu and P. Chen, *ACS Nano*, 2016, **10**, 3622.

19 P. Joshi, S. Kundu, S. Sanghi and D. Sarkar, *Smart Drug Delivery System*, InTech, 2016, ch. 7, DOI: DOI: 10.5772/61932.

20 Z. Wang, J. Yu, X. Zhang, N. Li, B. Liu, Y. Li, Y. Wang, W. Wang, Y. Li, L. Zhang, S. Dissanayake, S. Suib and L. Sun, *ACS Appl. Mater. Interfaces*, 2016, **8**, 1434.

21 A. Suryawanshi, M. Biswal, D. Mhamane, R. Gokhale, S. Patil, D. Guin and S. Ogale, *Nanoscale*, 2014, **6**, 11664.

22 M. Xue, Z. Zhan, M. Zou, L. Zhang and S. Zhao, *New J. Chem.*, 2016, **40**, 1698.

23 Z. Ding, F. Li, J. Wen, X. Wang and R. Sun, *Green Chem.*, 2018, **20**, 1383.

24 M. Liu, L. Yang, R. Li, B. Chen, H. Liu and C. Huang, *Green Chem.*, 2017, **19**, 3611.

25 Q. Lu, C. Wu, D. Liu, H. Wang, W. Su, H. Li, Y. Zhang and S. Yao, *Green Chem.*, 2017, **19**, 900.

26 G. Wang, Q. Guo, D. Chen, Z. Liu, X. Zheng, A. Xu, S. Yang and G. Ding, *ACS Appl. Mater. Interfaces*, 2018, **10**, 5750.

27 M. Xu, Z. Li, X. Zhu, N. Hu, H. Wei, Z. Yang and Y. Zhang, *Nano Biomed. Eng.*, 2013, 5(2), 65–71.

28 L. Li, G. Wu, G. Yang, J. Peng, J. Zhao and J. Zhu, *Nanoscale*, 2013, **5**, 4015.

29 L. Wang, Y. Wang, T. Xu, H. Liao, C. Yao, Y. Liu, Z. Li, Z. Chen, D. Pan, L. Sun and M. Wu, *Nat. Commun.*, 2014, **5**, 5357.

30 Y. Liu and D. Kim, *Chem. Commun.*, 2015, **51**, 4176.

31 M. Nurunnabi, Z. Khatun, K. Huh, S. Park, D. Lee, K. Cho and Y. Lee, *ACS Nano*, 2013, **7**, 6858.

32 K. Hyun and N. Saito, *Sci. Rep.*, 2017, **7**, 3825.

33 S. Kundu, R. Yadav, T. Narayanan, M. Shelke, R. Vajtai, P. Ajayan and V. Pillai, *Nanoscale*, 2015, **7**, 11515.

34 E. Hwang, H. Hwang, Y. Shin, Y. Yoon, H. Lee, J. Yang, S. Bak and H. Lee, *Sci. Rep.*, 2016, **6**, 39448.

35 C. Huang, C. Huang, F. Mai, C. Yen, S. Tzing, H. Hsieh, Y. Ling and J. Chang, *J. Mater. Chem. B*, 2015, **3**, 651.

36 D. Qu, M. Zheng, J. Li, Z. Xie and Z. Sun, *Light: Sci. Appl.*, 2015, **4**, e364.

37 R. Zhang, J. Adsetts, Y. Nie, X. Sun and Z. Ding, *Carbon*, 2018, **129**, 45.

38 H. Ding, S. Yu, J. Wei and H. Xiong, *ACS Nano*, 2015, **10**, 484.

39 G. Bharathi, D. Nataraj, S. Premkumar, M. Sowmiya, K. Senthilkumar, T. Thangadurai, O. Khyzhun, M. Gupta, D. Phase, N. Patra, S. Jha and D. Bhattacharyya, *Sci. Rep.*, 2017, **7**, 10850.

40 M. Cianchetti, C. Laschi, A. Menciassi and P. Dario, *Nat. Rev. Mater.*, 2018, **3**, 143–153.

41 M. Björnmalm, K. Thurecht, M. Michael, A. Scott and F. Caruso, *ACS Nano*, 2017, **11**, 9594.

42 X. Zheng, A. Than, A. Ananthanaraya, D. Kim and P. Chen, *ACS Nano*, 2013, **7**, 6278.

43 S. Bian, C. Shen, H. Hua, L. Zhou, H. Zhu, F. Xi, J. Liu and X. Dong, *RSC Adv.*, 2016, **6**, 69977.

44 Y. Shin, J. Lee, J. Yang, J. Park, K. Lee, S. Kim, Y. Park and H. Lee, *Small*, 2013, **10**, 866.

45 E. Nelson, *J. Am. Chem. Soc.*, 1929, **51**, 2808.

46 J. Tuček, P. Błoński, Z. Sofer, P. Šimek, M. Petr, M. Pumera, M. Otyepka and R. Zbořil, *Adv. Mater.*, 2016, **28**, 5139.

47 S. Li, Y. Li, J. Cao, J. Zhu, L. Fan and X. Li, *Anal. Chem.*, 2014, **86**, 10201.

48 M. Irimia-Vladu, *Chem. Soc. Rev.*, 2014, **43**, 588.

49 A. Robertson and J. Warner, *Nano Lett.*, 2011, **11**, 1182.

50 O. Kwon, H. Song, J. Conde, H. Kim, N. Artzi and J. Kim, *ACS Nano*, 2016, **10**, 1512.

51 A. Nair and S. Jacob, *J. Basic Clin. Pharm.*, 2016, **7**, 27.

52 J. Howe, C. Rawn, L. Jones and H. Ow, *Powder Diffr.*, 2003, **18**, 150.

53 L. Tang, R. Ji, X. Cao, J. Lin, H. Jiang, X. Li, K. Teng, C. Luk, S. Zeng, J. Hao and S. Lau, *ACS Nano*, 2012, **6**, 5102.

54 L. Malfatti, T. Kidchob, D. Aiello, R. Aiello, F. Testa and P. Innocenzi, *J. Phys. Chem. C*, 2008, **112**, 16225.

55 P. Elvati, E. Baumeister and A. Violi, *RSC Adv.*, 2017, **7**, 17704.

56 I. Jeon, S. Bae, J. Seo and J. Baek, *Adv. Funct. Mater.*, 2015, **25**, 6961.

57 K. Ganesan, S. Ghosh, N. Gopala Krishna, S. Ilango, M. Kamruddin and A. Tyagi, *Phys. Chem. Chem. Phys.*, 2016, **18**, 22160.

58 C. Chua, Z. Sofer, P. Šimek, O. Jankovský, K. Klímová, S. Bakardjieva, Š. Hrdličková Kučková and M. Pumera, *ACS Nano*, 2015, **9**, 2548.

59 S. Paulo, E. Palomares and E. Martinez-Ferrero, *Nanomaterials*, 2016, **6**(9), 157.

60 S. Song, M. Jang, J. Chung, S. Jin, B. Kim, S. Hur, S. Yoo, Y. Cho and S. Jeon, *Adv. Opt. Mater.*, 2014, **2**(11), 1016–1023.

61 G. Yang, C. Wu, X. Luo, X. Liu, Y. Gao, P. Wu, C. Cai and S. Saavedra, *J. Phys. Chem. C*, 2018, **122**(11), 6483–6492.

62 D. Wang, J. Chen and L. Dai, *Part. Part. Syst. Charact.*, 2014, **32**(5), 515–523.

63 R. Nair, R. Thomas, V. Sankar, H. Muhammad, M. Dong and S. Pillai, *ACS Omega*, 2017, **2**(11), 8051–8061.

64 T. Kumpulainen, A. Rosspeintner and E. Vauthey, *Phys. Chem. Chem. Phys.*, 2017, **19**, 8815.

65 S. Maiti, S. Kundu, C. Roy, T. Das and A. Saha, *Langmuir*, 2017, **33**, 14634.

66 E. Polo, M. Collado, B. Pelaz and P. del Pino, *ACS Nano*, 2017, **11**, 2397.

67 R. Gonzalez and R. Woods, *Digital image processing*, Pearson Education, Delhi, 2003.

68 P. Soille, *Morphological image analysis*, Springer, Berlin, 1999.

69 Dual Band Excitation: DAPI-FITC, *Nikon's MicroscopyU*, 2018, (accessed June 2018).

70 J. Zhao and M. Stenzel, *Polym. Chem.*, 2018, **9**, 259.

71 D. Shao, J. Li, F. Guan, Y. Pan, X. Xiao, M. Zhang, H. Zhang and L. Chen, *Int. J. Nanomed.*, 2014, **9**, 5753.

72 S. Behzadi, V. Serpooshan, W. Tao, M. Hamaly, M. Alkawareek, E. Dreaden, D. Brown, A. Alkilany, O. Farokhzad and M. Mahmoudi, *Chem. Soc. Rev.*, 2017, **46**, 4218.

73 S. Conner and S. Schmid, *Nature*, 2003, **422**, 37.

74 M. Cokakli, E. Erdal, D. Nart, F. Yilmaz, O. Sagol, M. Kilic, S. Karademir and N. Atabey, *BMC Cancer*, 2009, **9**, 65.

75 A. Nel, L. Mädler, D. Velegol, T. Xia, E. Hoek, P. Somasundaran, F. Klaessig, V. Castranova and M. Thompson, *Nat. Mater.*, 2009, **8**, 543.

76 T. Martin and W. Jiang, *Biochim. Biophys. Acta, Biomembr.*, 2009, **1788**, 872.

77 W. Jiang, R. Bryce, D. Horrobin and R. Mansel, *Biochem. Biophys. Res. Commun.*, 1998, **244**, 414.